JOURNAL OF AIRCRAFT
Vol. 39, No. 5, September–October 2002

# Computational Modeling of Hovering Rotor and Wake Aerodynamics

Roger C. Strawn*
*U.S. Army Aviation and Missile Command, Moffett Field, California 94035-1000*
and
M. Jahed Djomehri†
*NASA Ames Research Center, Moffett Field, California 94035-1000*

**Steady-state Reynolds-averaged Navier–Stokes computations are presented for a range of UH-60A model-rotor test cases in hover. The computations are designed to assess grid-related effects on the numerical results and employ 1) structured overset grids with high resolution on the rotor blades, 2) a systematic variation of grid resolution in the rotor wake, and 3) a systematic variation of outer-boundary locations. Computed rotor performance values agree very well with experimental measurements and show little sensitivity to either grid resolution or outer-boundary locations. However, the computations uniformly overpredict the blade sectional thrust near the rotor tip. This overprediction of blade tip thrust is explained by an analysis of the circulation distribution in the computed rotor wake system.**

## Nomenclature

| | | |
|---|---|---|
| $a$ | = | vortex core radius, m |
| $a_\infty$ | = | freestream speed of sound, m/s |
| $C_Q$ | = | rotor torque coefficient, $Q/[\pi\rho_\infty R^3(\Omega R)^2]$ |
| $C_T$ | = | rotor thrust coefficient, $T/[\pi\rho_\infty R^2(\Omega R)^2]$ |
| $C_t$ | = | rotor blade sectional thrust coefficient, $(\mathrm{d}T/\mathrm{d}r)/[0.5c\rho_\infty(\Omega R)^2]$ |
| $c$ | = | nominal rotor blade chord, m |
| $c_f$ | = | wall skin-friction coefficient |
| FM | = | rotor figure of merit, $C_T\sqrt{(C_T/2)}/C_Q$ |
| $M_t$ | = | hover-tip Mach number, $(\Omega R)/a_\infty$ |
| $n$ | = | number of rotor blades |
| $Q$ | = | rotor torque, N · m |
| $R$ | = | rotor radius, m |
| $Re$ | = | flowfield Reynolds number based on $V_{\text{tip}}$ and $c$ |
| $r$ | = | spanwise distance along rotor, m |
| $T$ | = | rotor thrust, N |
| $V_{\text{tip}}$ | = | rotor tip speed, m/s |
| $x$ | = | coordinate direction along the rotor chord, m |
| $y$ | = | coordinate direction normal to a viscous surface |
| $y^+$ | = | turbulent wall coordinate, $yRe\sqrt{(c_f/2)}$ |
| $z$ | = | coordinate direction normal to the rotor disk, m |
| $\Gamma$ | = | vortex circulation strength, $m^2/s$ |
| $\rho_\infty$ | = | freestream fluid density, $kg/m^3$ |
| $\Omega$ | = | rotor angular velocity, rad/s |

## Introduction

ALMOST all of the aerodynamic design problems associated with rotorcraft involve interactions between the rotating blades and their aerodynamic wake systems. Prediction of the rotor wake is one of the most challenging problems in rotorcraft computational fluid dynamics (CFD). Typically, the computed vortical wakes diffuse too rapidly due to grid-related numerical dissipation. For general unsteady rotor flowfields, current numerical schemes and computational grids are unable to preserve the vortices long enough to predict accurately the noise and airloads caused by blade–vortex interactions.

Hovering rotor problems are generally less computationally demanding than their forward-flight counterparts because they have periodic and steady-state solutions in the rotor frame of reference. As such, they are better suited for rotor wake grid-resolution studies. The general question for this paper is whether rotorcraft CFD methods can model hovering-rotor performance with solutions that are grid independent. Clearly, these grid-independent solutions must be accurate as well.

References 1–10 contain a sampling of published results for hovering-rotor CFD simulations. None of these simulations provides a rigorous demonstration of grid independence in the final results. By grid independence, we require that two separate results with substantially different grid resolutions produce the same results for rotor performance [$C_T$, $C_Q$, and figure of merit (FM)]. Ideally, two grids that are substantially different should have mesh spacings that differ by a factor of two in each direction. This requirement leads to a factor-of-eight difference in the number of points for the two grids and places severe demands on available computational resources.

Wake and Baeder[3] provide the most complete comparisons to date of Navier–Stokes CFD predictions and experimental hover-performance data. They present extensive comparisons of their computed results to the Lorber et al.[11] experimental data. Lorber et al. tested a 17.5% scale model UH-60A rotor and also a 3:1 tapered tip rotor in hover. In addition to overall thrust, torque, and FM, the experimental data contain blade sectional loading and measured blade elastic twist. The resulting data provide a detailed and comprehensive study of a high-performance rotor in hover.

Although Wake and Baeder's[3] computed results showed reasonably good correlation with the experimental data, they used coarse grids by today's standards. Their analysis used two different single-block grids consisting of 452,000 and 918,000 mesh points, respectively. At the time, a 918,000 point grid stretched the limits of available computational resources. However, Wake and Baeder recommended improved rotor wake grids and higher-accuracy numerical methods for future calculations.

Over the past few years, new CFD techniques for hovering rotors have been developed (Refs. 9 and 10). This current work builds

Received 24 April 2001; revision received 28 March 2002; accepted for publication 15 April 2002. 

*Research Scientist, Army/NASA Rotorcraft Division, Army Aeroflightdynamics Directorate; rstrawn@mail.arc.nasa.gov.
†Senior Research Scientist, Computer Sciences Corporation; djomehri@nas.nasa.gov.

on the efforts of Wake and Baeder[3] by applying improved numerical methods and much finer grids to recompute the Lorber et al.[11] UH-60A, model-rotor test cases. The objective is to control the grid resolution and boundary conditions carefully, to assess current computational capabilities for modeling hovering rotors.

## Computational Method

The Reynolds-averaged Navier–Stokes flow solver used in this study is based on a version of the OVERFLOW code developed by Buning et al.[12] OVERFLOW is a general-purpose Navier–Stokes code designed for fixed-wing overset-grid computations on static grids. Meakin[13] has generalized this code to accommodate arbitrary relative motion between vehicle components and to facilitate off-body solution adaption. The modified code automatically organizes grid components into groups of approximately equal size. This groupwise structure has been exploited to facilitate efficient parallel computations of multibody problems on scalable computer platforms.[14] On parallel machines, each processor is assigned a group of grids for computation, with intergroup communications performed using the message passing interface protocol. This code is known as OVERFLOW-D and has been extensively tested on IBM-SP and SGI Origin 2000 parallel computers.

The solution of hovering-rotor problems requires a number of modifications to the OVERFLOW-D flow solver. Reference 10 describes these modifications in detail, but the highlights are given hereafter.

### Rotational Grid Motion

Hovering rotors can take advantage of the flowfield being steady when viewed from a blade-fixed reference frame. The source-term formulation from Chen et al.[15] is used to convert the rotating-blade Navier–Stokes equations to a steady-state problem. Steady-state solutions require much less computational effort than their unsteady counterparts, thus allowing for finer grids to capture the details of rotor wakes in hover.

### Grid Overlaps

Two-cell overlaps have been added between adjacent grids. The basic version of OVERFLOW-D uses second-order spatial differencing with one-cell overlaps between adjacent grids. This approach ensures the continuity of flowfield information from one grid to the next; however, it does not allow flowfield derivative information to pass accurately between overlapping grids. To improve the accuracy of the overset-grid approach, a two-cell overlap option has been added to OVERFLOW-D. This two-cell overlap effectively allows the exchange of both flowfield data and flowfield gradient data between overlapping grids. It also allows the flow solver to be upgraded to a uniform fourth-order spatial-differencing scheme throughout the computational domain. This fourth-order scheme was used for all of the computations in this paper.

### Periodicity

Periodicity allows for significant computational savings by modeling only a portion of the multibladed rotor domain. Our implementation of periodicity in OVERFLOW-D uses two layers of ghost cells at both the periodic inflow and periodic outflow boundaries. These ghost cells match point to point with their periodic counterparts in the interior of the computational domain, and these periodic counterparts need not be located on the same processor. The ghost cells are updated from interior points at the corresponding periodic boundary following each iteration for the flow solver.

### Hovering-Rotor Grid System

OVERFLOW-D provides for automatic generation of off-body grids that are compatible with the near-body surface grids. These off-body grids surround the near-body grids with uniform resolution and gradually become coarser on approaching the computational outer boundaries. Despite this convenience of automatic grid generation, additional control over the placement and spacing of the off-body grids is required to improve the rotor wake resolution and to implement periodic boundary conditions for hovering

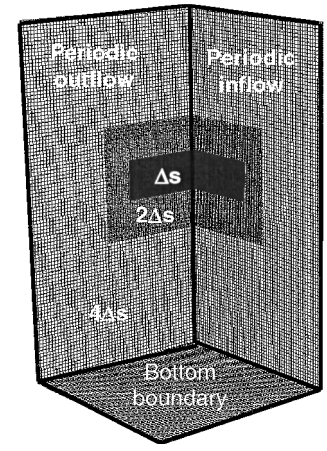


**a) Off-body**

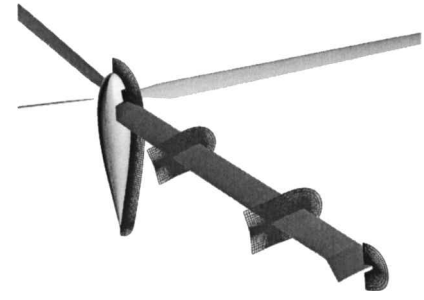

**b) Near-body grid systems**

**Fig. 1 UH-60A model rotor blade.**

rotors. This requirement for greater control led to the development of the off-body grid system shown in Fig. 1a for the UH-60A model rotor. Because this experimental rotor has four identical rotor blades, periodicity is used to reduce the size of the computational domain.

In Fig. 1a, a representative off-body grid with Cartesian uniform grid spacing surrounds the near blade region. If the spacing of this level one grid near the rotor blade is $\Delta s$, the spacing of the next surrounding level two grid is $2\Delta s$. The grid spacing continues to double for successive levels of off-body grids out to the computational outer boundary. The strategy of doubling the grid spacing for each higher off-body grid level allows one to place the outer grid boundaries far away from the rotor blade with an efficient distribution of grid points.

The outer-boundary location is controlled with a one-parameter value that specifies the distance from the top, bottom, and side boundaries to the blade tip. Baseline calculations for this paper were located six blade radii from the blade tip in all directions with five levels of off-body grid spacing.

Figure 1b shows the four grid systems used to discretize the near-blade region. The blade hub has an inviscid surface boundary condition with a $149 \times 29 \times 30$ mesh in the longitudinal, azimuthal, and normal directions. The presence of the hub provides an important blockage effect that prevents the root vortices from rising above the rotor plane (Ref. 10).

The blade tip and root cap grids each contain $129 \times 29 \times 55$ grid points, and the C–H grid on the main part of the rotor blade contains $209 \times 112 \times 55$ grid points in the chordwise, spanwise, and normal directions on the rotor. All near-body grids extend approximately 0.6 chord lengths beyond the blade and hub surfaces in all directions. Overall, the four baseline near-body grids have a total of $2.1 \times 10^6$ grid points. In addition to the geometric twist on the rotor blade, the computational model also includes the experimentally measured coning angle and elastic twist for each rotor thrust condition. All viscous meshes have their first grid point off of the wall located at $y^+ < 1$. The first three grid points away from the viscous surfaces have uniform normal spacing.

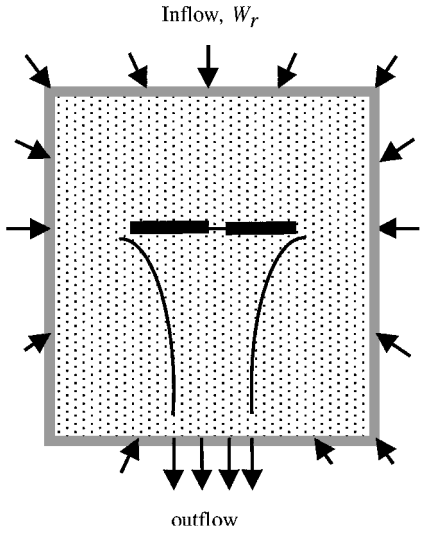


**Fig. 2 Source-sink boundary idealization for a hovering rotor system.**

#### Hover Boundary Conditions

The choice of boundary conditions for a given problem must satisfy two criteria. First, the boundary conditions must reasonably approximate the physical problem. Second, the boundary conditions must be compatible with characteristic wave propagation theory for the Euler and Navier–Stokes equations. Compatibility with characteristic theory prevents the buildup of numerical instabilities at the boundaries.

Most of the hovering-rotor calculations in Refs. 1–10 specify the outer-boundary values with an approximate source-sink condition shown in Fig. 2. As described in Ref. 2, the rotor outflow below the rotor blade can be idealized by one-dimensional momentum theory:

$$W_e = -2M_t\sqrt{C_T/2} \tag{1}$$

The radius of this outflow velocity region is given by $R/\sqrt{2}$. However, in the present implementation, the outflow velocity in Eq. (1) is not prescribed directly at the bottom boundary. It is simply used to estimate the inflow boundary values.

For inflow, a point sink of mass models the flow into the computational domain. This sink is located at the rotor hub, and its strength is adjusted to compensate for the estimated outflow given by Eq. (1). This condition results in an inflow velocity $W_r$ toward the hub at all boundaries:

$$W_r = -(M_t/4)\sqrt{(C_T/2)}(R/r)^2 \tag{2}$$

By the use of these inflow velocities, compatible density and pressure fields can be generated using isentropic relations between the boundary flowfield and stagnation flow at infinity. These inflow boundary values are then combined with values from the flowfield interior by prescribing the external entropy, tangential velocity, incoming Riemann invariant, and extrapolating the outgoing Riemann invariant from the interior.

For the outflow boundary, freestream pressure is prescribed, and all other quantities are extrapolated from the interior. The resulting mass outflow automatically adjusts to match the inflow. Thus, it is not necessary to prescribe the outflow velocities at the bottom boundary.

There is very little sensitivity in the final results to the value of $C_T$ used in the boundary condition Eqs. (1) and (2). Typically, the boundary condition $C_T$ value is adjusted to match the computed blade value during the calculation. However, using a constant boundary condition $C_T$ value from the experimental measurements produces virtually the same hover performance results.

These inflow–outflow boundary conditions provide a reasonably realistic approximation of the physical boundary and allow for a smaller computational domain than would otherwise be required with prescribed zero-velocity conditions at the outer boundaries. The philosophy is similar to an experimental hover chamber, where doors or slats are opened in the ceiling and floor to help prevent recirculation in the rotor wake. In general, the use of this source-sink boundary condition helps to stabilize the rotor wake in the CFD computation and speed up convergence to a steady-state result.

## Computational Results

The UH-60A model-rotor hover performance was computed at eight different collective angles. All cases were run at the same hover tip Mach number, which provided for significant compressibility at the blade tips. The exact value of this hover-tip Mach number and all experimental collective angles are subject to U.S. Army data restrictions. As mentioned earlier, the measured blade elastic twist was included in the grid generation for each case. Each computation used the near-body grid system described earlier, and the baseline off-body grids used a uniform level-one grid spacing (near the rotor) equal to 0.1 chord. Four additional off-body grid levels pushed the outer boundary locations to six radii beyond the blade tip in all directions.

The baseline calculations used a total of $10.6 \times 10^6$ grid points. In addition, one of the moderate collective-angle cases was run with the same $2.1 \times 10^6$ point near-field grids, but with $64 \times 10^6$ total grid points and a uniform level-one off-body grid spacing of 0.05 chords. Typical $10.6 \times 10^6$ grid point computations were run on 32 processors of an SGI Origin 2000 parallel computer. Overall thrust on the rotor was used to monitor the convergence to steady state for the calculation.

Figure 3 shows a sample convergence plot for a typical case. Typical calculations were run for 20,000–25,000 iterations, although thrust and torque values show little change after 15,000 iterations. The code requires 35 h on 32 SGI Origin processors to complete 20,000 iterations, resulting in approximately 1120 processor hours for each $10.6 \times 10^6$ grid-point case. The $64 \times 10^6$ grid-point case required 138 h on 112 SGI Origin processors and approximately 40,000 iterations for convergence. Total computational time for this case was about 15,500 processor hours.

#### Overall Rotor Performance

Figure 4 presents overall thrust and power results for the UH-60A model rotor. Figure 4 shows excellent agreement between experiment and computation for all but the lowest computed thrust level at $C_T = 0.0022$. For $C_T$ levels below 0.002, the rotor wake descends very slowly, and the computational results either converge very slowly, or not at all, due to the close proximity of the rotor wake system. These cases should be run with an unsteady CFD code to obtain time-averaged results.

Note that the 64 million grid-point solution shows good agreement with both the $10.6 \times 10^6$ grid-point computations and also with the experimental data. The overall predicted rotor performance is grid independent in the sense that it does not change when the rotor wake grid spacing is cut in half.

The FM plot in Fig. 5 provides a more sensitive comparison of computational and experimental performance results. FM serves as a ratio of ideal to actual rotor power. In Fig. 5, the maximum

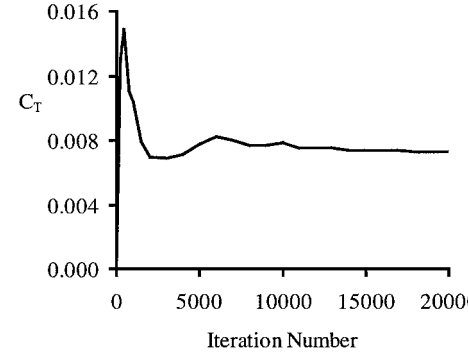


**Fig. 3 Typical thrust convergence history for a $10.6 \times 10^6$ grid point solution.**

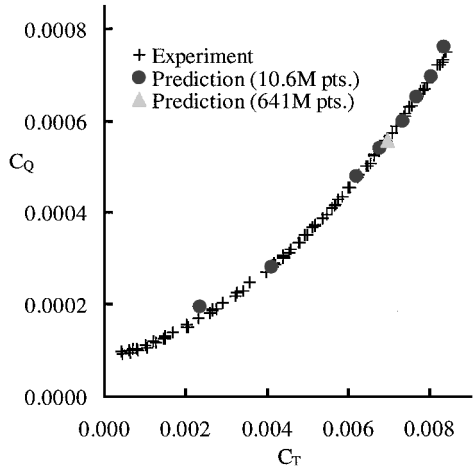


**Fig. 4 Thrust and power results for the UH-60A model rotor.**

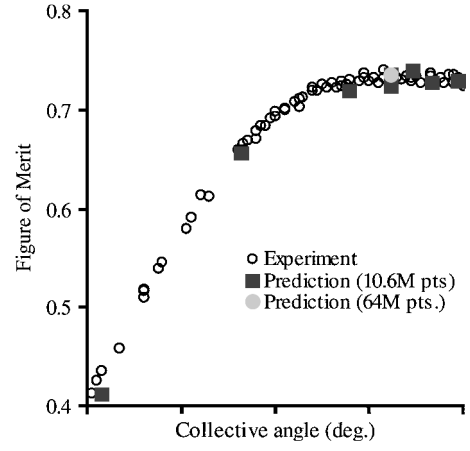


**Fig. 5 FM results for the UH-60A model rotor.**

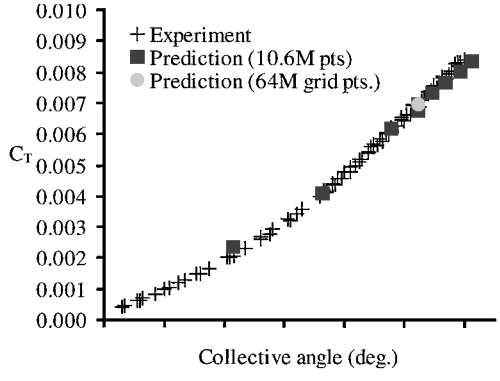


**Fig. 6 Rotor thrust as a function of collective angle.**

differences between experimental and computed FM are less than 0.02. The FM values for the $10.6 \times 10^6$ and $64 \times 10^6$ grid-point calculations match quite well, indicating that overall rotor performance has little sensitivity to the rotor wake grid resolution beyond $10.6 \times 10^6$ grid points.

Figure 6 presents a final measure of computed and experimental performance results. Here, the rotor thrust is plotted as a function of blade collective angle. Again, the computed results show good agreement with the experimental values.

### Blade Sectional Quantities

In addition to overall rotor performance, Lorber et al.[11] also measured the radial distributions of thrust along the rotor blades. Figure 7 compares the computed and experimental radial thrust distributions for a low and a high thrust case. U.S. Army data restrictions preclude

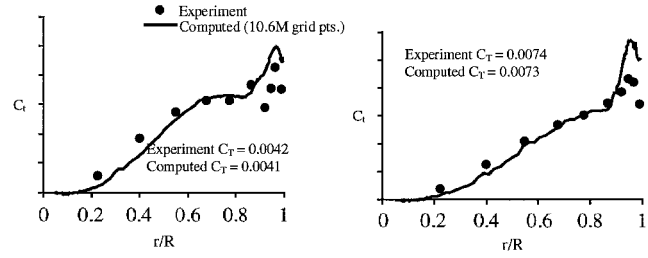


**Fig. 7 Sectional thrust distributions for two thrust conditions.**

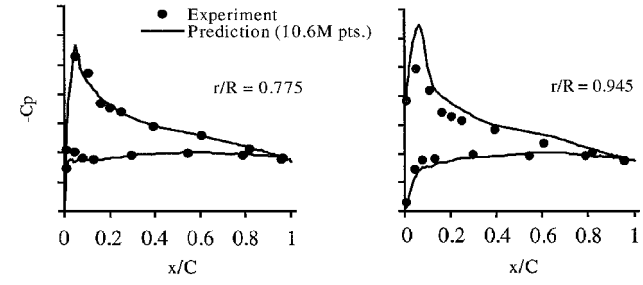


**Fig. 8 Chordwise pressure distributions at two radial stations (experimental $C_T = 0.0074$).**

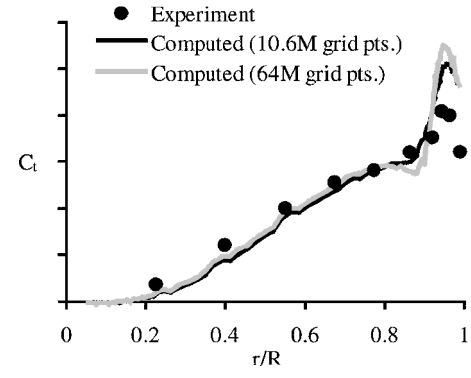


**Fig. 9 Comparison of sectional $C_t$ predictions for two different grid resolutions in the rotor wake.**

including the vertical scale numbers for all sectional quantities. For each case in Fig. 7, reasonably good agreement between experiment and computation is seen over much of the blade, except for the tip, where the rotor thrust is overpredicted in both cases. This overprediction of thrust at the rotor tip is common to all of the computed results.

Figure 8 shows blade sectional surface pressures at two spanwise locations for the high-thrust case. Note that the computed pressures show good agreement with the data for $r/R = 0.775$, where the $C_t$ value matches the experimental result in Fig. 7. At $r/R = 0.945$, the overprediction of $Ct$ is reflected in the overprediction of the pressures at this location. The shape of the computed pressure plot at $r/R = 0.945$ is consistent with a wake-induced inflow angle that is too high.

Figure 9 compares the sectional blade thrust for the $10.6 \times 10^6$ and $64 \times 10^6$ grid-point calculations with experimental data for a moderate thrust case. Both predictions are consistent with Fig. 8 in that they show an overprediction of thrust near the blade tip. Two important conclusions can be drawn here. First, the two computed results show similar sectional thrust distributions except near the blade tip. Second, although the changes in grid density affect the blade-tip loading, these tip-loading changes do not substantially change the overall blade performance, as evidenced in Figs. 4–6.

The finer-grid case has less grid-related dissipation in the rotor wake, and the tip vortices should have higher peak-to-peak velocities than their coarser-grid counterparts. Given similar vortex trajectories, these higher peak-to-peak velocities should cause slightly more

**Table 1 Experimental and computed performance for the UH-60A model rotor**

| Conditions | $C_T$ | $C_Q$ | FM |
|---|---|---|---|
| Experiment | 0.00706 | 0.000572 | 0.73 |
| $2R$ BC[a] | 0.00689 | 0.000558 | 0.72 |
| $3R$ BC | 0.00668 | 0.000548 | 0.70 |
| $6R$ BC | 0.00675 | 0.000542 | 0.72 |
| $9R$ BC | 0.00674 | 0.000547 | 0.72 |

[a]Boundary conditions.

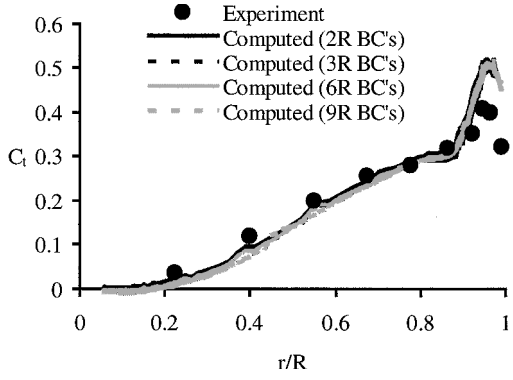


**Fig. 10 Computed sectional thrust with different computational boundary locations ($10.6 \times 10^6$ grid points).**

upwash near the blade tip and more downwash inboard of the first vortex passage below the rotor. These expectations are consistent with the Fig. 9 results near the radial location of the first vortex passage ($r/R = 0.9$). Everywhere else, the two computations show similar results for sectional thrust.

### Boundary Condition Effects

One important issue is whether the hovering-rotor boundary conditions described earlier have a significant effect on the computed results. Boundary condition effects can be estimated by running the same hover calculation and systematically varying the outer-boundary locations. All computations keep the same blade geometry, near-body rotor and hub grids and off-body level-one grid. The outer boundary locations are varied by altering the sizes of the off-body grids for levels two and above.

Figure 10 shows computed and experimental blade sectional thrust for the moderate thrust case. Computed results are presented for cases with outer boundaries located 2, 3, 6, and 9 blade radii from the rotor tip in all directions. As shown in Fig. 10, the boundary locations have little effect on the blade sectional thrust distributions.

The overall rotor performance for these four boundary locations is presented in Table 1. Note that the blade $C_T$ and $C_Q$ values show little change beyond the $3R$ boundary locations. Because these large changes in boundary location have little effect on the computations, it is assumed that the implementation of the hovering rotor boundary conditions, described earlier, also has little effect on the computed results. As a rule, the outer computational boundary locations should be located at least $3R$ from the rotor blade tip in all directions.

### Rotor Wake Geometry

Lorber et al.[11] presented experimental measurements for the wake geometry (vertical descent and radial contraction) for many of their test cases. In addition to the experimental data points, they also present approximate generalized curve fits for the experimental wake trajectories.

Figures 11 and 12 show the Lorber et al.[11] derived wake trajectories for the moderate thrust case. Also shown in Figs. 11 and 12 are computed results from the $64 \times 10^6$ grid-point simulation of the same case. Computational vortex centers were determined by analyzing contours of vorticity magnitude on two-dimensional azimuthal wake cuts behind the rotor blade. The vortex centers

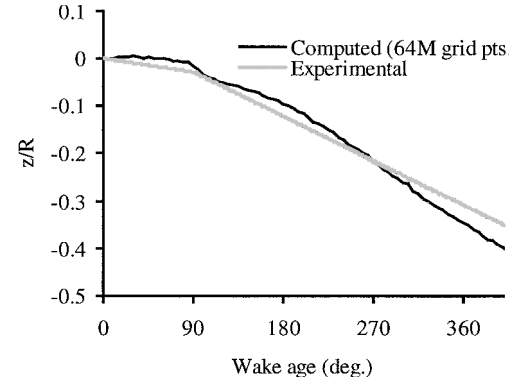


**Fig. 11 Vertical tip-vortex descent.**

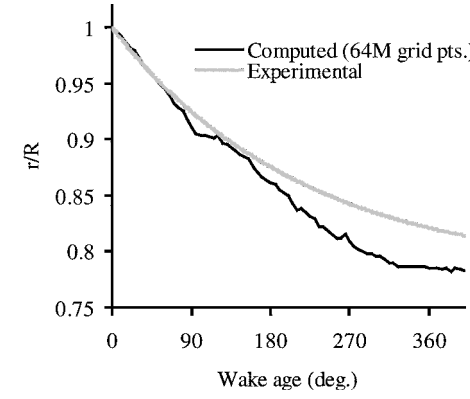


**Fig. 12 Tip-vortex radial contraction.**

coincide with local maxima in vorticity magnitude. Both the experimental curves and the computed results contain a fair amount of uncertainty in their plotted values.

Despite these uncertainties, generally good agreement is seen between the experimental and computational vortex trajectories. A key factor in these hovering rotor simulations is the vertical miss distance between the tip vortex and the rotor blade at 90 deg wake age. In Fig. 11, the experimental value for this miss distance is approximately $0.4c$, and the computed value is about $0.2c$. Thus, the computed vortex passes slightly closer to the rotor blade at 90 deg wake age. After this point, however, the vertical decent rates are very similar.

For the radial contraction in Fig. 12, the experimental and computational trajectories are very close through 180 deg of wake age. After this point, the computed vortex shows more contraction than the experimental result. One possible explanation for this discrepancy is that the floor of the experimental test facility was located only $3R$ below the plane of the rotor. A small ground effect in the experiment could have reduced the contraction in the experimental wake system, whereas the outflow boundary conditions in the computation are much closer to a free-air environment.

The $10.6 \times 10^6$ grid-point result at the moderate thrust condition has virtually the same vortex trajectory as the $64 \times 10^6$ grid-point result. Vortex centers are much more difficult to pick out from the coarser-grid results, however. Figure 13 shows a comparison of vorticity magnitude contours for this case on a cutting plane that is 60 deg behind the rotor blade. Note that the $64 \times 10^6$ grid-point rotor wake shows much higher peak vorticity levels than the $10.6 \times 10^6$ computation. Also, four or five individual vortices are seen in the $64 \times 10^6$ grid-point result, whereas the $10.6 \times 10^6$ result only shows two distinct vortices.

Figure 14 shows a section of the computed vortex wake system on the $64 \times 10^6$ grid. The vortex sheets plus a number of individual tip vortices are shown. The vortex sheets descend much faster than the tip vortices, which is consistent with experimental observations. Figure 14 also shows that the tip vortices distort as they descend in the wake. As they descend, they lose their symmetry because they

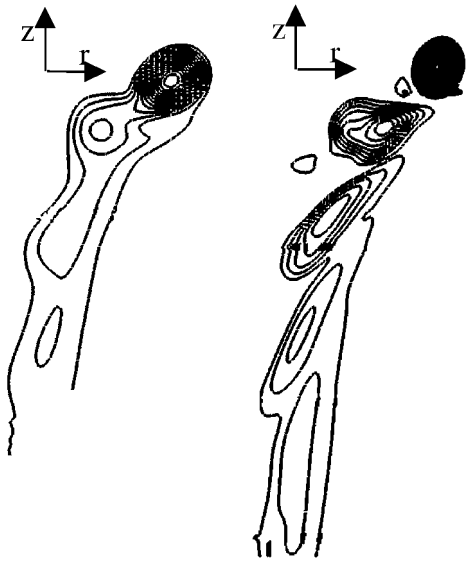


a) 10.6 M grid pts b) 64 M grid pts

**Fig. 13 Uniformly spaced contours of vorticity magnitude for the UH-60A model rotor on a 60-deg cutting plane behind the rotor blade.**

**Fig. 14 Computed vorticity magnitude contours on a cutting plane located 45 deg behind the rotor blade ($64 \times 10^6$ grid points).**

are subject to a shearing force at the edge of the vortex-induced downwash.

#### Effect of Turbulence Models

All computations shown thus far used the OVERFLOW-D implementation of the Baldwin–Barth[16] one-equation turbulence model. This model solves a turbulent transport equation for eddy viscosity with damping functions added in the near-wall regions.

In addition, the moderate thrust case was also computed using the Baldwin–Lomax[17] algebraic turbulence model. This computation used the same $10.6 \times 10^6$ grid that was used for the Baldwin–Barth[16] calculations. Figure 15 compares the sectional thrust distributions on the rotor blade for the two cases. The Baldwin–Lomax[17] model predicts a much higher peak sectional thrust value near the rotor tip, with much lower sectional thrust toward the rotor hub. The overall integrated thrust and power for the Baldwin–Lomax model also differ substantially from the Baldwin–Barth[16] result.

To put these computational differences into perspective, both turbulence models were developed primarily to match two-dimensional boundary-layer physics. In addition, the computations solve the thin-layer Navier–Stokes equations, which means that they only model viscous forces normal to the rotor surface.

Our hovering rotor calculations are much more complex than this assumed two-dimensional boundary-layer physics. First, the

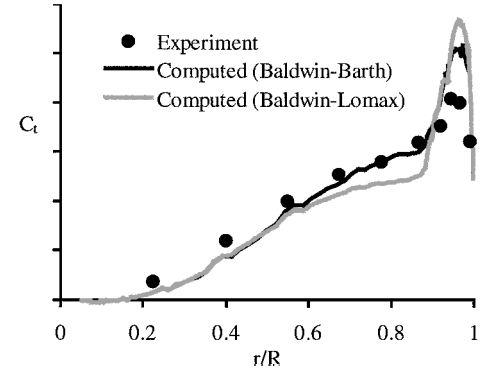


**Fig. 15 Comparison of sectional thrust for two turbulence models ($10.6 \times 10^6$ grid points).**

tip-vortex rollup process is highly three dimensional. Both turbulence models have difficulties modeling this type of three dimensionality, and typical grid systems cannot resolve it because they only use viscous spacing in the direction normal to the blade surface. Second, in our calculations, the vortex at 90 deg wake age passes very close below the following rotor blade. Part of this tip vortex interacts with the rotor boundary layers, embedding streamwise vorticity and adding three dimensionality to the flowfield near the rotor tip.

In general, one-equation turbulence models such as Baldwin–Barth[16] are more robust than the Baldwin–Lomax[17] algebraic model for complex geometries and three-dimensional flowfields. The Baldwin–Lomax model uses the near-wall vorticity distribution to obtain a turbulent length scale, and this vorticity distribution is clearly affected by the close proximity of the preceding blade vortex.

## Analysis and Discussion

A major outstanding question for the computed results is why they consistently overpredict the sectional thrust near the blade tip compared to the experimental data. Usually, it is tempting to attribute these discrepancies to CFD grid problems such as boundary-condition effects, grid skewness, or lack of wake resolution. However, the computations in this paper were designed to address these grid-related issues directly and to eliminate them as potential problems.

One possible cause for these sectional thrust discrepancies is the difference in computed and experimental miss distance between the tip vortex and the rotor blade at 90 deg wake age. The experimental vortex passes under the rotor by $0.4c$ and the computation shows it passing under the rotor by $0.2c$. The smaller miss distance in the computation may cause enough additional upwash near the rotor tip to explain the loading discrepancies between experiment and computation.

To address this question, a Scully[18] velocity distribution was used to model the tip vortex and to estimate the change in induced angle of attack on the rotor at $r/R = 0.95$ when the vortex miss distance is moved from $0.2c$ to $0.4c$. Differences in $C_t$ at $r/R = 0.95$ were then estimated from these induced angle-of-attack changes.

In this test, the 90-deg wake age vortex passes beneath the rotor at $r/R = 0.90$, and the vortex strength $\Gamma$ was approximated two ways. First, it was estimated from the computed maximum bound circulation on the rotor, and second, it was estimated by integrating the vorticity around a two-dimensional azimuthal slice of the CFD-computed vortex. Sectional lift changes on the blade were then estimated from simple two-dimensional linear aerodynamic theory. Both estimates used the computed value of $0.4c$ for the vortex core. With these assumptions, the change in vortex miss distance only accounts for about 25% of the experimental and computational $C_t$ discrepancies at $r/R = 0.95$ that are seen in Figs. 9 and 10. If anything, one would expect three dimensionality to further diminish these estimated miss-distance effects.

If not the vortex miss distance, then a more likely explanation for the overprediction of rotor tip thrust involves the interaction between the first vortex passage beneath the rotor and the vortex

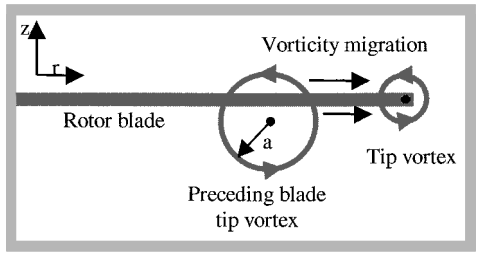


**Fig. 16 Possible mechanism for vorticity transfer from preceding blade vortex to newly developing tip-vortex.**

rollup at the blade tip. In the $64 \times 10^6$ grid-point calculation, the vortex rotational core size is approximately $0.4c$ at 90 deg wake age. The computed vortex radius at this point is about double what one expects to see in the physical problem. This larger computed size is presumably caused by grid-related diffusion. The center of this vortex passes beneath the following blade at about $r/R = 0.90$, with a vertical miss distance of $0.2c$. A comparison of this vertical miss distance to the vortex core radius indicates that a substantial rotational portion of the vortex hits the blade and/or passes above it. In the experiment, this interaction probably does not occur because the rotational vortex core radius is smaller, and the vertical miss distance is greater.

Figure 16 shows a possible explanation for this situation. When the preceding blade vortex hits the rotor, its vorticity merges with the boundary layer and part of it migrates along with the trailing vortex sheet toward the newly developing tip vortex. Thus, the newly developing tip vortex gets a boost in circulation, whereas the preceding blade vortex loses circulation in this transfer. As a result, the new tip vortex has a higher circulation value and, most likely, a larger rotational core size. The higher circulation means that its subsequent interaction with the following rotor blade provides more induced upwash near the blade tip, leading to higher sectional thrust there. This proposed explanation assumes that the total circulation in a vortex is generally conserved. Even when the vortex core size increases due to numerical dissipation, the integrated vortex circulation should remain constant.

Although this hypothesis cannot be proven directly, three observations from the computed results support this explanation. All three observations rely on numerical integrations of vorticity to obtain the circulation in the tip vortices. These integrations were performed on two-dimensional cutting planes at various azimuthal angle locations behind the rotor blade, such as the one shown in Fig. 13b. These integrations are most accurate when the grid resolution is high, and so the $64 \times 10^6$ grid-point case was used for most of our numerical results.

The first observation is that the computed tip vortex circulation for <90 deg wake age is higher than one would predict from the blade loading distribution. Assuming that all of the blade bound circulation rolls up into the tip vortex, one would estimate a vortex strength, $\Gamma/(V_{\text{tip}}c)$, equal to 0.26. Integration of the computed results, however, gives a vortex strength of $0.335 \pm 0.030$, from 5 to 85 deg wake age, and these numbers are consistent with the hypothesis that the newly developed tip vortex has been augmented by the vortex circulation from the preceding blade.

The second observation is that the computed tip vortex strength drops from $0.335 \pm 0.03$ to $0.22 \pm 0.06$ after its first passage beneath the following blade. Because circulation for the overall vortex wake system must be conserved, the obvious question is, "Where did the circulation go after the first blade–vortex interaction at 90 deg wake age?" Most likely, it migrates through the shear layer to augment the circulation in the newly formed vortex at the rotor blade tip.

A third observation from the computations offers an explanation for the large differences in blade loading for the two different turbulence models in Fig. 15. When the circulation values are compared for the first two vortices in the cutting plane shown in Fig. 13b, the Baldwin–Barth[16] result gives values of 0.335 and 0.22 for the vortex strengths at 60 and 150 deg wake age, respectively. By contrast, the Baldwin–Lomax[17] result gives vortex strengths equal to 0.43 and 0.16 for these same two vortices. The Baldwin–Lomax computation has a stronger vortex at <90 deg wake age, and a weaker one at >90 deg wake age. The choice of turbulence model probably affects the amount of vorticity that migrates from the inboard to the outboard vortex in Fig. 16. Thus, the Baldwin–Lomax result has a higher vortex strength for <90 deg wake age, and this leads to the stronger interaction with the following rotor blade as shown in Fig. 15.

## Conclusions

Calculations in this paper have been designed specifically to address numerical issues for hovering rotors. Near-body grids use consistent high-density viscous meshes with substantial variations in rotor wake grid size to assess the solution quality. Uniform fourth-order central differencing has been added to OVERFLOW-D to further improve the numerical accuracy. The computed results have been tested over a wide range of outer-boundary locations.

The good news is that overall integrated rotor performance agrees very well with experimental measurements and shows little sensitivity to either grid resolution or outer-boundary locations. In this sense, the results in this paper demonstrate that careful attention to numerical grids and boundary conditions can provide grid-independent results for integrated rotor loads.

The bad news is that the computations consistently overpredict the blade sectional thrust distributions near the rotor tip. An explanation is postulated for this sectional-thrust overprediction in terms of vorticity migration and is backed up with integrated vortex circulation values from the computed results. One way to study this phenomenon in more detail would be to use a simpler CFD geometry, such as a vortex generator placed upstream of a fixed wing.

The computations point to two possibilities for improving the agreement between computed and experimental radial loading distributions. First, a small increase in the computed vortex miss distance at 90 deg wake age should significantly reduce the migration of vorticity toward the developing tip vortex and improve the correlations with the experiment. Obviously, unresolved modeling issues in the computation may affect the vortex miss distance; however, the test facility in the experiment may also have an influence on the rotor wake geometry.

Lorber et al.[11] performed their experiment in a test facility 4.5 rotor diameters wide, 6.3 diam long, and 3.2 diam high. Louvers and doors in the walls were opened to minimize the effects of rotor wake recirculation. This test facility is considerably smaller than the computational domain for the calculations. One way to estimate the facility effects on the near-wake geometry would be to run the CFD calculation with outer-boundary conditions and locations that more closely match those in the experimental facility.

A second possibility for correlation improvement centers on reducing the vortex rotational core size for <90 deg wake age. A smaller vortex core would minimize the viscous interaction with the following rotor blade and prevent the migration of vorticity toward the newly forming tip vortex.

Certainly, grid-related diffusion plays a role in causing our computed vortex cores to be larger than their experimental counterparts. However, lack of grid resolution is probably not the only cause for the overprediction of vortex core size. The computed results indicate that, once the tip vortex has fully rolled up (>15 deg wake age), its core size does not change appreciably until it hits the following blade. Perhaps it is the entrainment of additional vorticity from the inboard blade–vortex interaction that enlarges the vortex core at its inception. This brings us back to vortex miss distance and turbulence modeling issues.

Resolution of these questions requires additional focused studies on the combined effects of turbulence models, grid size, and outer-boundary modeling. In spite of these outstanding issues, quite a bit has been learned from this study regarding grid and boundary condition effects for rotary-wing CFD hover performance and blade loading computations. These lessons provide an overall assessment and understanding of the quality of our current numerical simulations. They also help to focus our future efforts on research areas with a high payoff toward improved solution accuracy.

## References

[1]Srinivasan, G. R., Baeder, J. D., Obayashi, S., and McCroskey, W. J., "Flowfield of a Lifting Rotor in Hover: A Navier–Stokes Simulation," *AIAA Journal*, Vol. 30, No. 10, 1992, pp. 2371–2378.

[2]Srinivasan, G. R., Raghavan, V., Duque, E. P. N., and McCroskey, W. J., "Flowfield Analysis of Modern Helicopter Rotors in Hover by Navier–Stokes Method," *Journal of the American Helicopter Society*, Vol. 38, No. 3, 1993, pp. 1–11.

[3]Wake, B. E., and Baeder, J. D., "Evaluation of a Navier–Stokes Analysis Method for Hover Performance Prediction," *Journal of the American Helicopter Society*, Vol. 41, No. 1, 1996, pp. 1–17.

[4]Duque, E. P. N., and Srinivasan, G. R., "Numerical Simulation of a Hovering Rotor Using Embedded Grids," *Proceedings of the 48th Annual Forum*, American Helicopter Society, June 1992, pp. 429–445.

[5]Hariharan, N., and Sankar, L. N., "Application of ENO Schemes to Rotary-Wing Problems," AIAA Paper 95-1892, July 1995.

[6]Strawn, R. C., and Barth, T. J., "A Finite-Volume Euler Solver for Computing Rotary-Wing Aerodynamics on Unstructured Meshes," *Journal of the American Helicopter Society*, Vol. 38, No. 2, 1993, pp. 61–67.

[7]Bottasso, C. L., and Shephard, M. S., "Parallel Adaptive Finite Element Euler Flow Solver for Rotary Wing Aerodynamics," *AIAA Journal*, Vol. 35, No. 6, 1997, pp. 937–944.

[8]Dindar, M., Lemnios, A., Shephard, M., and Jansen, K., "Effect of Tip–Vortex Resolution on UH-60-A Rotor-Blade Hover Performance Calculations," *Proceedings of the 54th Annual Forum*, American Helicopter Society International, May 1998, pp. 45–57.

[9]Ahmad, J., and Strawn, R. C., "Hovering Rotor and Wake Calculations with an Overset-Grid Navier–Stokes Solver," American Helicopter Society, 55th Annual Forum, May 1999, pp. 1949–1959.

[10]Strawn, R. C., and Ahmad, J. U., "Computational Modeling of Hovering Rotors and Wakes," AIAA Paper 2000-0110, Jan. 2000.

[11]Lorber, P. F., Stauter, R. C., and Landgrebe, A. J., "A Comprehensive Hover Test of the Airloads and Airflow of an Extensively Instrumented Model Helicoper Rotor," *Proceedings of the 45th Annual Forum*, American Helicopter Society, May 1989, pp. 281–295; also U.S. Army Aviation Systems Command, AVSCOM TR 91-D-16C, Vols. 1–5, Moffett Field, CA, March 1992.

[12]Buning, P. G., Jesperson, D. C., Pulliam, T. H., Chan, W. M., Slotnick, J. P., Krist, S. E., and Renze, K. J., "OVERFOW User's Manual, Version 1.8g," NASA Langley Research Center, Moffett Field, CA, March 1999.

[13]Meakin, R., "Composite Overset Structured Grids," *Handbook of Grid Generation*, edited by J. F. Thompson, B. K. Soni, and N. P. Weatherill, CRC Press, Washington, DC, 1999, pp. 11-1–11-19.

[14]Meakin, R. L., and Wissink, A. M., "Unsteady Aerodynamic Simulation of Static and Moving Bodies Using Scalable Computers," *A Collection of the 14th AIAA Computational Fluid Dynamics Conference*, TP AIAA-99-3302, AIAA, Norfolk, VA, 1999, pp. 469–483.

[15]Chen, C. L., McCroskey, W. J., and Obayashi, S., "Numerical Solutions of Forward-Flight Rotor Flows Using an Upwind Method," *Journal of Aircraft*, Vol. 28, No. 6, 1991, pp. 374–380.

[16]Baldwin, B. S., and Barth, T. J., "A One-Equation Turbulence Transport Model for High Reynolds Number Wall-Bounded Flows," NASA TM 102847, Aug. 1990.

[17]Baldwin, B. S., and Lomax, H., "Thin Layer Approximation and Algebraic Model for Separated Turbulent Flows," AIAA Paper 78-0257, Jan. 1978.

[18]Scully, M. P., "Computation of Helicopter Rotor Wake Geometry and Its Influence on Rotor Harmonic Airloads," Massachusetts Inst. of Technology, Atomspheric Sciences Research Lab., TR 178-1, Cambridge, MA, March 1975.